

Article

Mineral Composite Plaster Containing Hollow Glass Microspheres and CSA Cement for Building Insulation

Stefan Zelder ^{1,*} , Andreas Rosin ¹ , Dominik Helling ¹, Thorsten Gerdes ¹, Friedbert Scharfe ² and Stefan Schafföner ¹ 

¹ Faculty of Engineering Science, University of Bayreuth, Keylab Glass Technology, Chair of Ceramic Materials Engineering, Prof.-Rüdiger-Bormann-Str. 1, D-95447 Bayreuth, Germany; andreas.rosin@uni-bayreuth.de (A.R.); dominik.helling@uni-bayreuth.de (D.H.); thorsten.gerdes@uni-bayreuth.de (T.G.); stefan.schaffoener@uni-bayreuth.de (S.S.)

² Franken Maxit Mauermörtel GmbH & Co., Azendorf 63, D-95359 Kasendorf, Germany; Friedbert.Scharfe@maxit.de

* Correspondence: stefan.zelder@uni-bayreuth.de

Featured Application: This publication describes a mineral-based insulating plaster sprayable on a façade.

Abstract: Renovation of old buildings plays a key role in the sustainable energy transition because they are often poorly insulated and, therefore, lose a lot of heat through walls and ceilings. An important measure of renovation is façade insulation. Established and widely used materials include rigid expanded polystyrene (EPS) and extruded polystyrene (XPS) insulation boards. However, these boards do not easily follow the form of non-planar surfaces such as individually formed, ornamented, or bent façades. Furthermore, fire protection of these boards requires the addition of, for example, hazardous brominated flame retardants that impede recycling. This paper investigates a novel alternative insulating composite plaster. It is purely inorganic and can be applied easily by casting or wet spraying to any wall or ceiling element. The composite material consists of only two components: micro hollow glass microspheres as the insulating light component and calcium sulfoaluminate cement as the binder. Various compositions containing these components were cast, hydraulically set, and characterized with respect to microstructure, phase development during hydration, and thermal conductivity. With an increasing amount of hollow glass spheres, the density decreased to less than $0.2 \text{ g}\cdot\text{cm}^{-3}$, and the thermal conductivity reached 0.04 to $0.05 \text{ W}\cdot\text{m}^{-1}\text{K}^{-1}$, fulfilling the demands of building insulation.

Keywords: insulating plaster; calcium sulfoaluminate cement; hollow glass microspheres; thermal insulation; energetic renovation of buildings



Citation: Zelder, S.; Rosin, A.; Helling, D.; Gerdes, T.; Scharfe, F.; Schafföner, S. Mineral Composite Plaster Containing Hollow Glass Microspheres and CSA Cement for Building Insulation. *Appl. Sci.* **2022**, *12*, 1152. <https://doi.org/10.3390/app12031152>

Academic Editors: Jiří Zach and Jorge de Brito

Received: 23 December 2021

Accepted: 19 January 2022

Published: 22 January 2022

Publisher's Note: MDPI stays neutral with regard to jurisdictional claims in published maps and institutional affiliations.



Copyright: © 2022 by the authors. Licensee MDPI, Basel, Switzerland. This article is an open access article distributed under the terms and conditions of the Creative Commons Attribution (CC BY) license (<https://creativecommons.org/licenses/by/4.0/>).

1. Introduction

CO₂ emissions reduction is the most pressing topic to mitigate global warming. The European Green Deal sets the ambitious goal of a 55% reduction in greenhouse gas emissions by 2030 [1]. This applies in particular to the building sector. In the European Union, around 33% of greenhouse gases are currently emitted by buildings [2]. These are generated especially by the use of fossil fuels for heating. Therefore, CO₂ emissions can be lowered by improving building insulation in order to reduce heat losses through the building shell [3]. Since new buildings generally have good insulation, the impact of the energy-efficient renovation of old buildings is even greater [4]. Apart from the general need for better insulation of old buildings, renovation has to be sped up in order to meet the requirements of the European Union by 2030. The renovation rate is nowadays around 1% of the building stock per year, but it is estimated that this rate has to be at least doubled in the near future [5].

Building insulation materials range from purely mineral insulation materials, such as rock wool over polymer foams, such as EPS or XPS, to organic materials such as wooden or straw-based materials. EPS boards have a market share of about 80% in Europe [6] because of their low thermal conductivity ($0.035\text{--}0.049\text{ W}\cdot\text{m}^{-1}\text{K}^{-1}$) [7] and low density ($30\text{ kg}\cdot\text{m}^{-3}$) [8], which are combined with low costs. EPS boards are applied directly onto the wall, resulting in two challenges. First, planar boards need to be adjusted and fixed manually on the façade, which is labor- and time-intensive. Secondly, EPS boards must cover the entire façade to avoid thermal bridges, which is problematic for some older buildings as their façades are often uneven, decorated, or even landmarked. Since EPS boards cover and conceal any individual façade design, there is a growing interest in form-following materials and application techniques for façade renovation.

An attractive solution to these problems is a mineral-based composite insulation plaster that can be applied, for example, by wet spraying [9]. Earlier investigations on lightweight concrete reported an admixture of hollow glass microspheres embedded in a Portland cement and geopolymers cement matrix [10,11]. By embedding hollow glass microspheres (HGMSs) in concrete, the thermal conductivity and the density of the composite concrete were reduced. However, cement clinker production emits an average of 0.842 t of CO_2 for every ton of cement clinker [12]. Many of these emissions result from the calcination of limestone to produce Portland cement clinker [13]. Over the past few decades, several alternative cementitious binders have been developed [14]. One of them is calcium sulfoaluminate (CSA) cement. Its production emits only 50% of the CO_2 compared with Portland cement [15]. This is due to its limited lime content and the reduced firing temperature of the clinker of only $1250\text{ }^\circ\text{C}$ [16], which is 200 K lower than for Portland cement. In addition, CSA cement also settles very quickly [17]. This is mainly due to the formation of ettringite, which provides early strength. The shrinkage of CSA cement can be controlled by adjusting the sulfate content in the clinker [18]. After mixing with water, a transportable and processable mass is created. This mass can be conveyed through pipes using cement pumps and applied by plastering machines. These properties make CSA cement a superior binding agent for a mineral insulating plaster [9].

Based on the above considerations, this study investigated a composite plaster based on CSA cement and HGMSs only. Varying compositions of HGMSs and CSA cement were prepared by setting the amount of HGMSs from 0 to 70 wt.% in relation to the dry mass. After hydraulic setting, the mixtures were analyzed in order to report the thermal and mechanical properties as well as the phase composition.

2. Materials and Methods

2.1. Materials

The plaster mixtures were prepared by admixing the two components (CSA cement and hollow glass microspheres (HGMSs)) with water. CSA cement was used as the binding agent (Next Base Cement grey, Buzzi Unicem, Casale Monferrato, Italy). Its X-ray fluorescence analysis (XRF, ZSX Primus II, Rigaku, Japan) is provided in Table 1.

Table 1. Oxide composition of the CSA cement clinker used in this study determined by X-ray fluorescence analysis.

Element	CaO	Al ₂ O ₃	SO ₃	SiO ₂	Fe ₂ O ₃	TiO ₂	MgO	K ₂ O
Composition (wt.%)	45.7	23.5	19.5	6.3	2.4	1.3	1.0	0.3

Hollow glass microspheres (HGMSs) of type K15 from 3M Europe were used as the lightweight insulating component. According to the datasheet, the HGMSs are made of alkali-resistant borosilicate glass with a density of $0.15\text{ g}\cdot\text{cm}^{-3}$, a median diameter of $60\text{ }\mu\text{m}$, and a wall thickness of $1\text{--}2\text{ }\mu\text{m}$ [19].

CSA cement and HGMSs were mixed in the ratios presented in Table 2. A ratio of HGMSs higher than 70 wt.% was not feasible due to the low mechanical strength of the

hydrated material. Dry mixing of CSA cement and HGMSs was performed with a tumble mixer (Turbula T2F, WAB, Muttenz, Switzerland) at 47 rpm for 15 min to ensure a good mixture and to prevent segregation.

Table 2. Composition of the dry mixtures and the used w/c ratios.

Specimen	100C	90C	80C	70C	60C	50C	40C	30C
CSA cement in wt.% of dry matter	100%	90%	80%	70%	60%	50%	40%	30%
HGMSs in wt.% of dry matter	0%	10%	20%	30%	40%	50%	60%	70%
water/cement ratio	0.45	0.7	1.3	1.8	1.9	2.4	2.75	3

Since the content of the binding component varied with each mixture, the water/cement (w/c) ratio was increased stepwise in order to achieve good workability. The best w/c ratio for each mixture was determined individually by carefully adding tap water during continuous mixing. The maximum addition of water was reached as soon as the mixture stopped absorbing water, and excess water showed up at the surface, which is known as “bleeding”. The determined and used w/c ratios are summarized in Table 2. The prepared plaster mixtures were finally stirred for 1 min in a mixer (N50-619, Hobart, Offenburg, USA) according to the standard DIN EN 196-1 [20].

After mixing with tap water, the plaster was immediately cast into suitable molds. For each set of samples, six prisms with a $20 \times 20 \times 76 \text{ mm}^3$ edge length and one prism with a $134 \times 160 \times 40 \text{ mm}^3$ edge length were cast. Before casting, the molds were treated with rapeseed oil as a mold-release agent to prevent sticking after hydration. The small prisms (Figure 1a) were used to measure bending strengths, density, and porosity, while the larger samples were used to analyze thermal conductivity (Figure 1b).

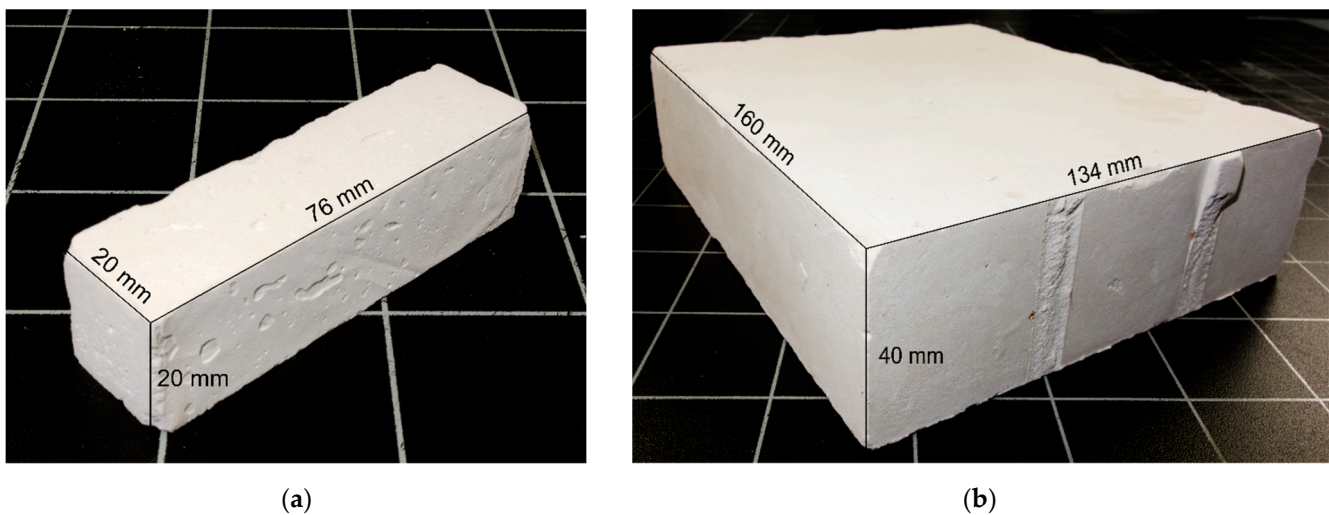


Figure 1. Specimen with 50 wt.% CSA cement (50C) after 14 days of hydration: (a) small prism; (b) big prism.

After casting, the molds were placed immediately on a vibrating table (Analysette 3 Spartan, Fritsch, Idar-Oberstein, Germany) for 1 min in order to achieve form fitting and to remove large bubbles. The amplitude was set to 1 mm. Afterwards, the molds were covered and stored inside a sealed cabinet at 99% relative humidity and 20°C . After 24 h, the specimens were demolded and stored inside the same cabinet for another 13 days.

2.2. Methods

Mechanical testing was performed using a universal testing machine (Inspect 5 Table Blue, Hegewald & Peschke, Nossen, Germany). According to the standard DIN EN 196-1 [20], the three-point bending tests had to be performed on wet specimens. The testing device was set to a traverse speed of 5 mm/min until a pre-load of 1 N was reached. The traverse speed was then immediately lowered to 2 mm/min. The termination criterion was reached when the measured force decreased by 80%. All measurements were conducted with a 1 kN load cell.

The density of the raw materials in powder form was determined using a helium pycnometer (AccuPyc™II 1340, Micromeritics, Norcross, GA, USA). Before measurement, the chamber was flushed 10 times by helium gas. The filling pressure was set to 134.45 kPa, and the measurement started when equilibrium was reached (<0.0345 kPa/min). A series of 10 measurements for each powder was performed [21].

The porosity of the cast specimens was measured using the Archimedes method. Before the measurement, the samples were stored in a drying chamber at 40 °C for at least 24 h. Then, the dry weight of the specimen was determined using a precision scale (AC 210 S, Satorius, Göttingen, Germany). The specimen was degassed inside a desiccator and evacuated for 30 min at a pressure of 10 mbar. Afterwards, deionized water with 50 ppm 2-octanol (Merck, Germany) was poured into the desiccator until the specimen was completely immersed. A cover with holes was placed above the specimen to prevent floating because the density of the specimen was expected to be lower than that of deionized water. After the addition of deionized water, the desiccator was evacuated for another 30 min before the lid was removed. The specimen was kept immersed at atmospheric pressure for at least 30 min. After infiltration, the buoyancy mass was determined. The weight of the wet sample was measured directly after removing the sample from the bath and blotting water with a wet towel.

The pore network and microstructure were investigated by scanning electron microscopy (SEM, Sigma 300 VP, Zeiss, Oberkochen, Germany). The hydrated specimens were dried at 40 °C for at least 24 h before SEM analysis. Each specimen was sputtered with gold (Sputter Coater 108 Auto, Cressington, Watford, England) at 30 mA for 60 s. The SEM analysis was performed with an acceleration voltage of 5 kV.

Phase analysis was carried out by X-ray diffractometry (XRD, D8 Discovery A25, Bruker, Billerica, MA, USA) with a copper radiation source (1.54060 Å) operating at 40 kV and 40 mA. The diffractograms were recorded using a Lynxeye detector. The measurement range of 2Θ was set from 10° to 60° with a time step of 0.2 s. During the measurement, the sample was rotated at a speed of 15 rpm. Rietveld refinement and phase analysis were performed with the open-source software Profex (Version 4.3.5) [22].

The thermal conductivity was measured using a surface and a needle probe (Isomet 2114, Applied Precision, Bratislava, Slovakia). Each specimen was dried in a drying chamber at 40 °C for 5 days before measurement. The measurement was conducted in an air-conditioned laboratory at 20 °C. Conductivity measurements were performed at three different spots on the large prisms.

3. Results and Discussion

3.1. Density and Microstructure

First, the pure density of the raw materials, i.e., CSA cement and hollow glass microspheres (HGMSs), was measured using helium pycnometry. The pure densities of HGMSs and CSA cement were found to be 0.142 g·cm⁻³ and 2.87 g·cm⁻³, respectively. The Archimedes measurement was performed on three specimens for each composition reported in Table 2. Equation (1) was used to calculate the open porosity (ϵ) of each specimen using the dry mass (m_{dry}), the buoyancy mass (m_{b}), and the mass of the water-infiltrated specimen (m_{wet}).

$$\epsilon = \frac{m_{\text{wet}} - m_{\text{dry}}}{m_{\text{wet}} - m_{\text{b}}} \quad (1)$$

Figure 2 illustrates the calculated open porosity for each plaster composition, starting with 100% cement at the left side. The open porosity, ϵ , changed slightly with a changing composition. The specimens with 100% and 90% cement (samples 100C and 90C) had open porosities of around $\epsilon = 25\%$. With an increasing HGMS content, the open porosity increased to $\epsilon = 32.7\%$ with 60% cement (sample 60C) but decreased slightly to $\epsilon = 30\%$ – 31% with further addition of HGMSs (samples 50C to 30C). Because the addition of HGMSs mainly contributes to closed porosity, the open porosity is generally not expected to be affected much by addition of HGMSs. Moreover, an open porosity of 26% is the void fraction of the densest sphere packing of uniformly sized spheres with a volume fraction of 74 vol.%. The increase in the void fraction above 30% as a function of the rising HGMS fraction was probably caused by remnants of the increasing water amount used for the plaster's preparation (see Table 3). Excess water, which is not used during hydration, accumulates in the voids until the specimen has dried. The evaporating water leaves pore space behind, which then contributes to the overall open porosity.

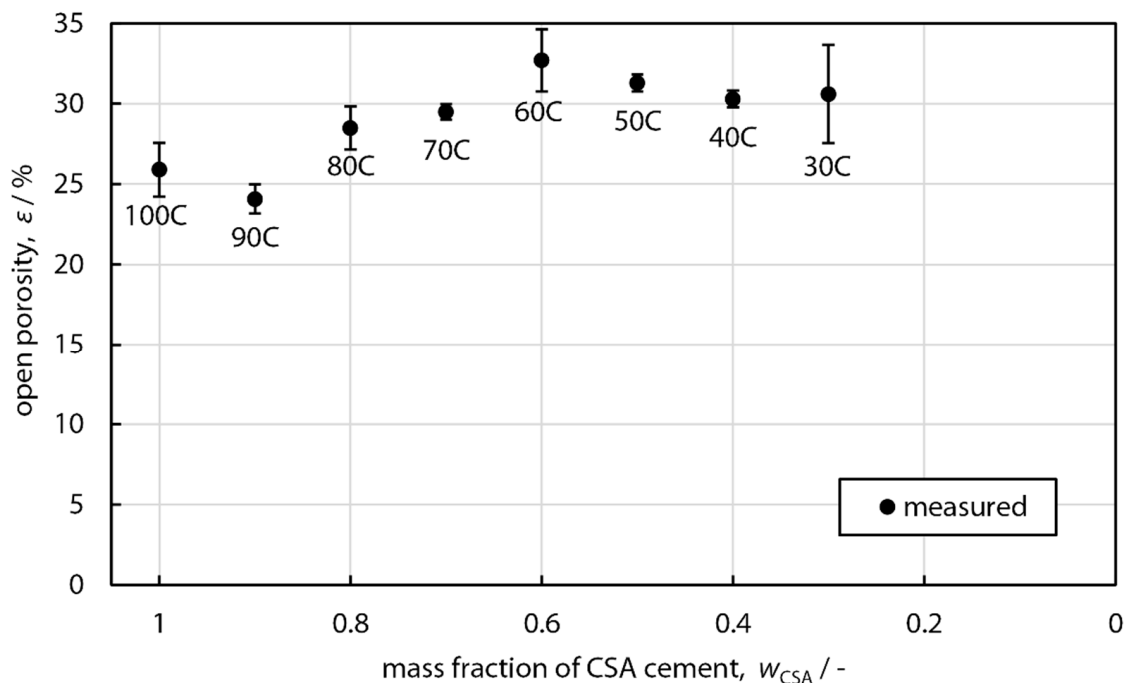


Figure 2. Open porosity measured using the Archimedes method for each sample composition using three specimens each ($N = 3$). The specimens were investigated after 14 days of hydration.

Table 3. Calculated volume fractions, ϕ_i , of CSA cement, HGMSs, and air as well as the calculated density of the hydrated and dried specimens according to open porosity.

Specimen	100C	90C	80C	70C	60C	50C	40C	30C
ϕ_{air} (vol.%)	25.9	24.1	28.5	29.5	32.7	31.3	30.3	30.6
ϕ_{HGMS} (vol.%)	0	48.3	57.1	61.4	61.5	64.6	66.9	67.6
ϕ_{CSA} (vol.%)	74.1	27.6	14.4	9.1	5.8	4.1	2.8	1.8
Density ($\text{g}\cdot\text{cm}^{-3}$)	1.63 ± 0.02	0.82 ± 0.01	0.44 ± 0.01	0.26 ± 0.02	0.23 ± 0.01	0.19 ± 0.02	0.16 ± 0.01	0.13 ± 0.01

The open porosity values and pure densities of the HGMSs as well as the pure density of hydrated CSA cement ($2.24 \text{ g}\cdot\text{cm}^{-3}$) were used to determine the real volume fractions (ϕ_i) of CSA cement and HGMSs with $\phi_{\text{air}} = \epsilon$, respectively. Table 3 shows the volume fractions ϕ_i for each specimen. The volume fraction of HGMSs reached 48.3% with an addition of only 10 wt.% of HGMSs (specimen 90C), and then increased to 67.6% in specimen 30C.

The bulk densities were determined according to the Archimedes method using Equation (2). The bulk densities (ρ) of the specimen were calculated from the dry mass (m_{dry}), the buoyancy mass (m_b), and the mass of the infiltrated specimen (m_{wet}). Since the infiltration medium is deionized water at 20 °C, the density ρ_b is 0.9982 g·cm⁻³.

$$\rho = \rho_b \cdot \frac{m_{dry}}{m_{wet} - m_b} \tag{2}$$

Figure 3 shows the development of the bulk density as a function of the volume fraction of CSA cement, ϕ_{CSA} . The direction of the x-axis is inverted, so the pure cement appears on the left side at $\phi = 1$, and all mixtures with HGMSs follow into the right direction with increasing HGMS content. Since the open porosity did not vary significantly, the decrease in bulk density can be mostly attributed to the addition of HGMSs. The highest bulk density was 1.66 g·cm⁻³ for sample 100C, whereas the lowest value was 0.15 g·cm⁻³ for sample 30C (Table 3). The data points in the diagram show almost a linear behavior of density over volume fraction.

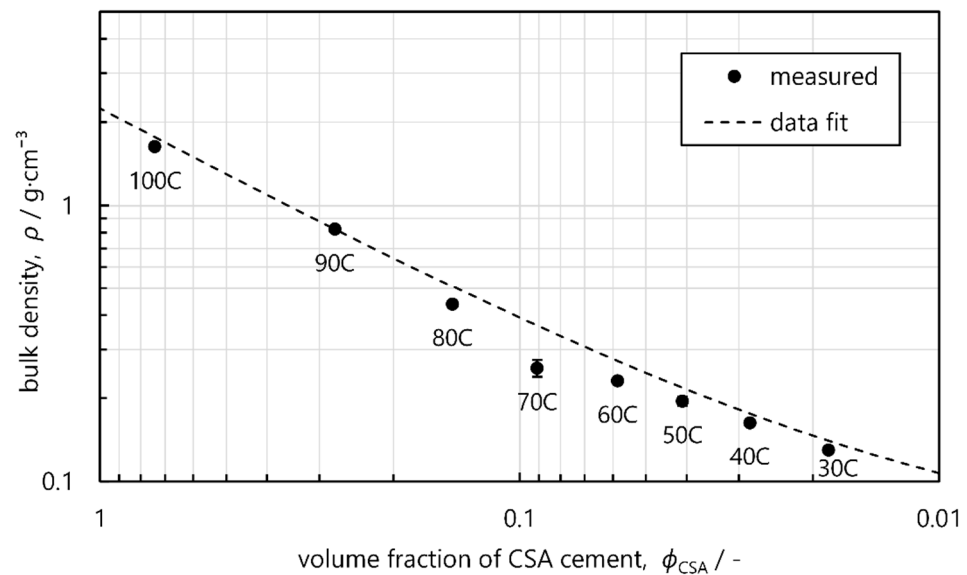


Figure 3. Calculated bulk density of each specimen based on Archimedes measurement. Data fit to $f(\phi) = a_0 + a \cdot \phi^v$, with $a_0 = 0.055$, $a = 2.184$, and $v = 0.81$.

Properties of composites containing two or more components are often described mathematically by a power law, here in the simplified form $f(x) = a_0 + a \cdot x^v$ with $x = [0, 1]$ for binary systems. The exponent, v , can be determined by the slope of the curve in double logarithmic diagrams. A data fit performed for the measured bulk densities shows an exponent of $v \approx 0.8$ if the composites are considered as a quasi-binary system and the contribution from air is neglected.

The microstructure and the adhesion between HGMSs and CSA cement were investigated with SEM. Figure 4a shows the as-received HGMSs without addition of concrete. The diameter of the spheres varied between 10 and 90 μm . Furthermore, very few spheres showed defects, such as being punctured or having completely destroyed shells. Since the HGMSs were not mixed or mechanically treated beforehand, these defects must originate from production, transport, or handling.

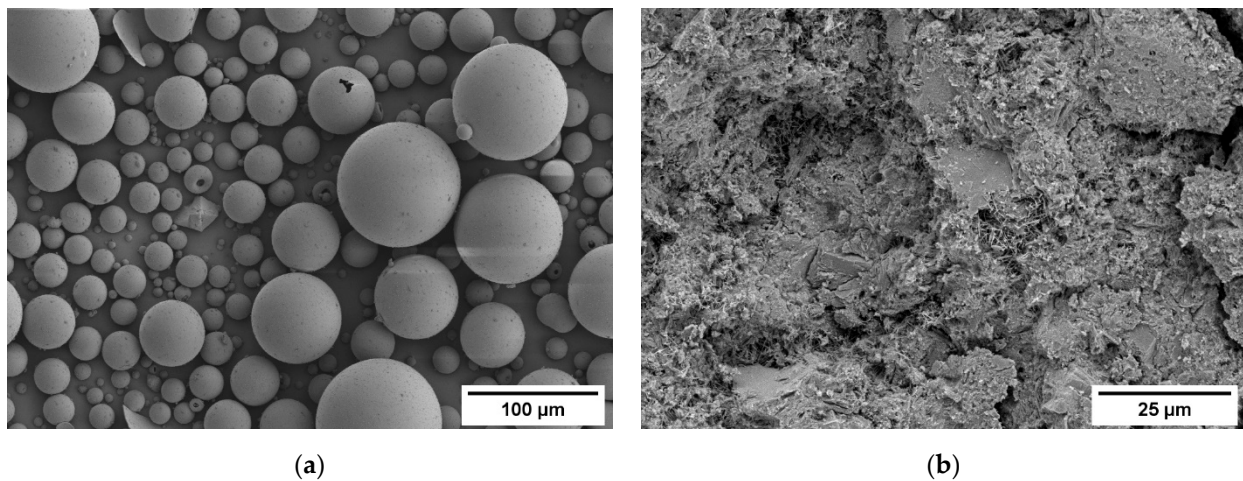


Figure 4. (a) SEM image of HGMSs. The acceleration voltage was set to 3 kV, while a SE detector was used. (b) SEM image of the hydrated CSA cement (sample 100C) after storage for 14 days in a moist atmosphere. The acceleration voltage was set to 5 kV, and again a SE detector was used.

Figure 4b shows an SEM image of a fractured surface of a CSA prism containing no HGMSs (sample 100C) after the flexural bending test. The specimen was prepared with a w/c ratio of 0.45 and hydrated for 14 days. The cracks that can be seen on the surface were most likely a result of the flexural bending test since no shrinkage was observed either after casting or after hydration. The sample showed a dense microstructure; needle-like crystals resulted from the formation of ettringite. Apart from ettringite crystals, clinker phases such as ye'elite and anhydrite might still have been present due to an incomplete hydration reaction. Thus, XRD measurements were used to analyze the degree of hydration, which will be described in the last section.

Figure 5 shows SEM images for mixtures with 50 wt.% HGMSs (sample 50C) at different magnifications. The volume fraction of the CSA cement was just 3.2%, yet the HGMSs were smoothly embedded in the cement matrix, which was forming an extended, needle-like network due to the hydration reaction. To a large extent, the HGMSs were intact, which is a prerequisite for achieving excellent insulating properties.

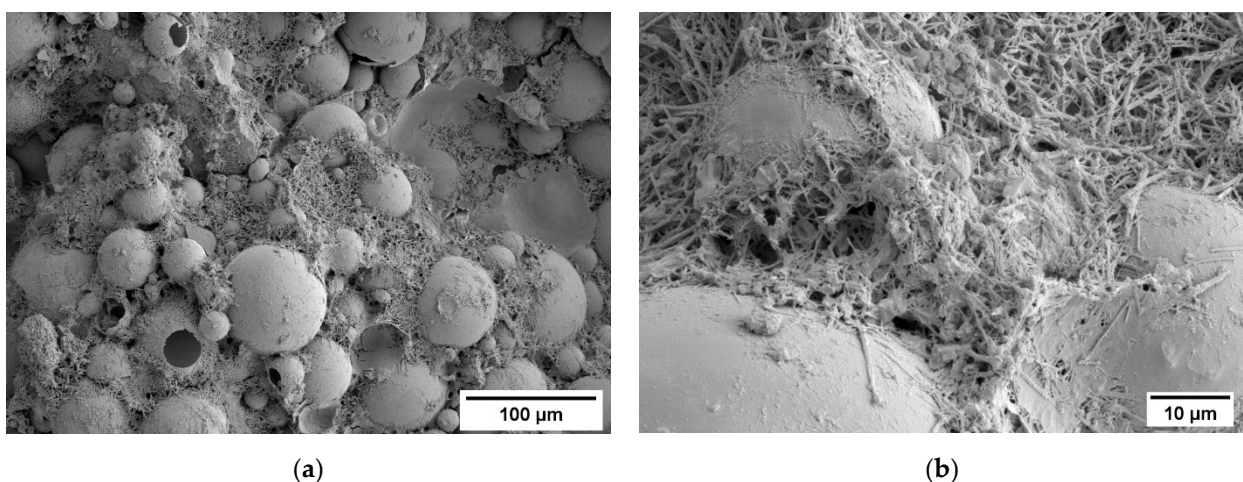


Figure 5. SEM images of sample 50C, stored for 14 days in a moist atmosphere. The acceleration voltage was set to 5 kV, using a SE detector: (a) magnification 250 \times ; (b) magnification 1500 \times .

The needle-like structures surrounding the HGMSs are characteristic for ettringite. This ettringite network provided a well-connected network and bonding between the cement phase and HGMSs. The ettringite matrix also contributed positively to the open

porosity and, hence, to a low thermal conductivity, but the addition of HGMSs probably lowered the mechanical properties in comparison with the pure CSA samples.

Figure 6 shows SEM images of sample 30C, with 70 wt.% HGMSs. The volume percentage of CSA cement was just 1.4 wt.%. The HGMSs were loosely stacked, and the void was scarcely filled with ettringite, but the hydration of the cement phase occurred obviously on the shells of the HGMSs, which helped to connect the HGMSs and created a durable network. However, in contrast to sample 50C, the long crystals in the network were missing. Figure 6b shows very few crystals with a pronounced needle-like structure (see, e.g., the top left corner). Apart from that, the number of broken shells seems to be slightly increasing compared with Figures 4 and 5. This could be attributed to an increased degree of shell breakage during preparation or during three-point bending tests, as shown by the SEM pictures of the fractured surfaces.

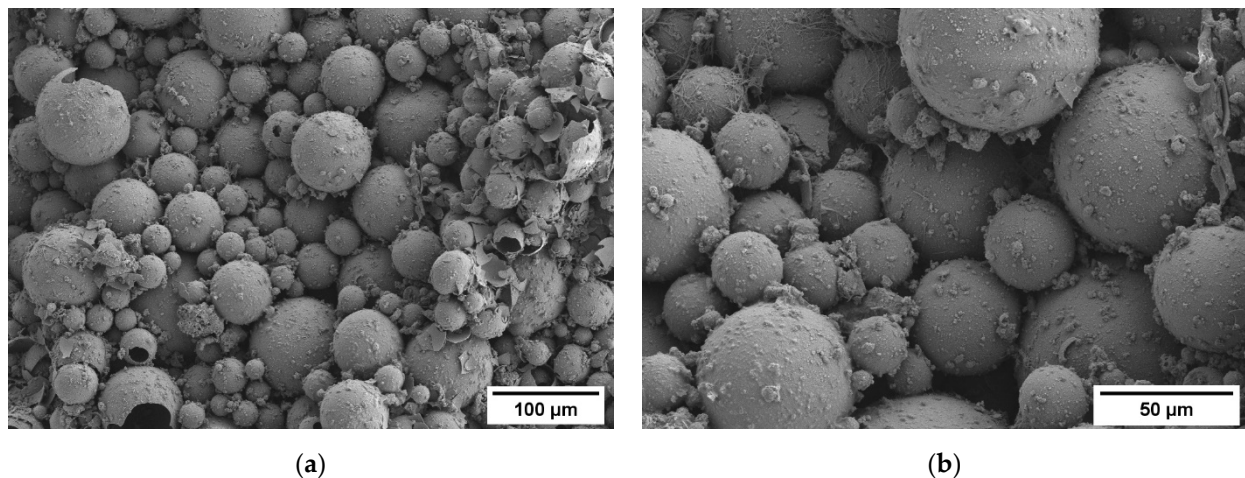


Figure 6. SEM images of a fractured surface after three-point bending tests of the hydrated sample 30C, with 70 wt.% HGMSs and 30 wt.% CSA cement. The acceleration voltage was set to 5 kV, while a SE detector was used: (a) magnification 200 \times ; (b) magnification 500 \times .

The three-point bending tests were carried out in a non-dried state according to DIN EN 196-1 [20]. All specimens were covered with a wet towel before testing to prevent them from drying. The results of the three-point bending tests are shown in Figure 7. Sample 100C showed the highest bending strength of 3.74 MPa. With an increased amount of HGMSs, the maximum bending strength decreased by more than 80% to 0.56 MPa for sample 70C, and even to 0.34 MPa for sample 30C (Table 4).

Table 4. Flexural strength and thermal conductivity for all mixtures.

Specimen	100C	90C	80C	70C	60C	50C	40C	30C
Flexural strength (MPa)	3.74 ± 0.36	2.30 ± 0.22	1.54 ± 0.29	0.56 ± 0.03	0.50 ± 0.09	0.57 ± 0.07	0.42 ± 0.06	0.34 ± 0.03
Thermal conductivity ($\text{W}\cdot\text{m}^{-1}\text{K}^{-1}$)	0.833 ± 0.024	0.186 ± 0.003	0.073 ± 0.002	0.072 ± 0.007	0.055 ± 0.001	0.048 ± 0.001	0.046 ± 0.001	0.043 ± 0.001

The rapid decrease in mechanical strength with the first addition of HGMSs indicates that the primary strength-providing component was the hydrated cement phase. As soon as the volume percentage of HGMSs rose to more than 60% (cf. Table 3, samples 70C to 30C), the flexural strength dropped to about one-tenth of the value of sample 100C. Beyond that point (70C), the volume fraction of HGMSs increased only slightly. Accordingly, the flexural strength only declined to a small extent.

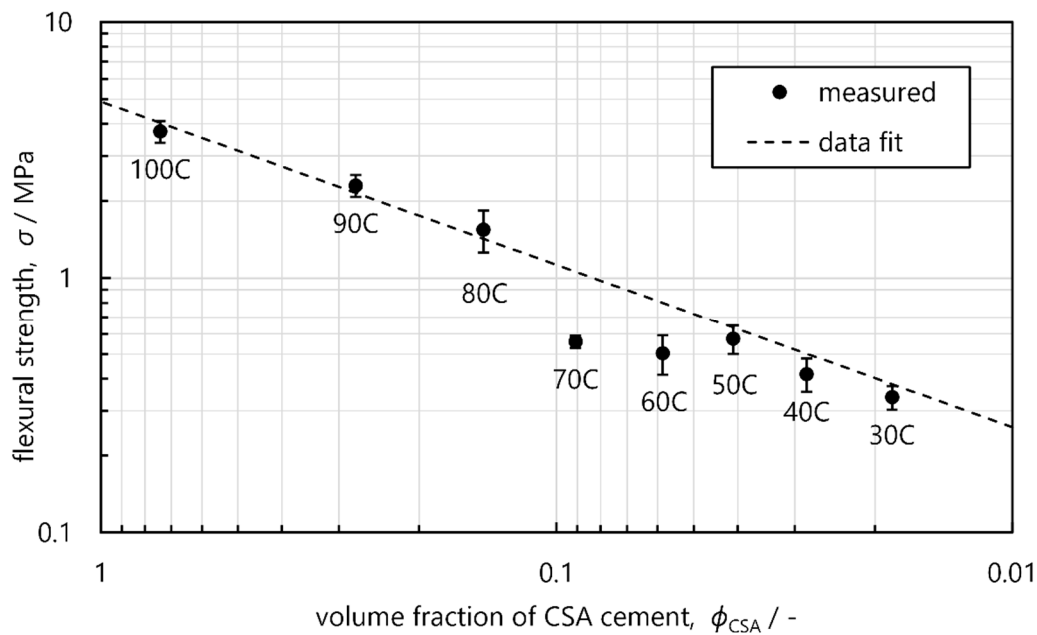


Figure 7. Three-point bending tests of the hydrated specimens. The specimens were tested after 14 days of hydration in a wet state. For each sample composition, six prisms were tested ($N = 6$). Data fit to $f(\phi) = a_0 + a \cdot \phi^v$, with $a_0 = 0$, $a = 4.892$, and $v = 0.638$.

3.2. Thermal Properties

The thermal conductivity was measured using a surface probe at room temperature. The specimens were stored in a drying chamber for five days before measurement to ensure that the samples were water-free.

Figure 8 shows the results of the measurements. Sample 100C exhibited the highest thermal conductivity of $0.83 \text{ W} \cdot \text{m}^{-1} \text{K}^{-1}$. Since the specimen contained an open porosity of about 26%, the thermal conductivity of the sample should include contributions from the CSA cement and air. With the addition of HGMSs, a third contribution had to be accounted for. Consequently, the thermal conductivity decreased with an increasing amount of HGMSs and accordingly a decreasing amount of cement. The lowest thermal conductivity was achieved for sample 30C. Its conductivity was $\lambda = 0.043 \text{ W} \cdot \text{m}^{-1} \text{K}^{-1}$ (Table 4). Given the fact that the open porosity for the specimens from 70C to 30C did not vary much (only 3.2% variation), the decrease in thermal conductivity can be exclusively explained by the insulating effect of the HGMSs. The HGMSs exhibit low-pressure conditions inside, which result in a very low internal heat transfer by means of convection, and heat conduction is limited due to their thin glass shell. In accordance, the thermal conductivity of the pure HGMSs was measured to be $0.0401 \text{ W} \cdot \text{m}^{-1} \text{K}^{-1}$ using a needle probe. As described, the spheres arrange themselves close to the densest sphere packing. It is therefore expected that the thermal conductivity of the HGMS/CSA composites would approach that of pure HGMSs with an increasing amount of HGMSs. According to the performed data fit in Figure 8, the infinite limit is $a_0 = 0.0404 \text{ W} \cdot \text{m}^{-1} \text{K}^{-1}$, which is in good agreement with the above value.

In order to achieve even lower thermal conductivity values (the conductivity of air is $0.026 \text{ W} \cdot \text{m}^{-1} \text{K}^{-1}$ [23]), an increase in open porosity would be required without losing the structural cohesion that is mainly provided by solid bridges between HGMSs and the cement's crystalline phases.

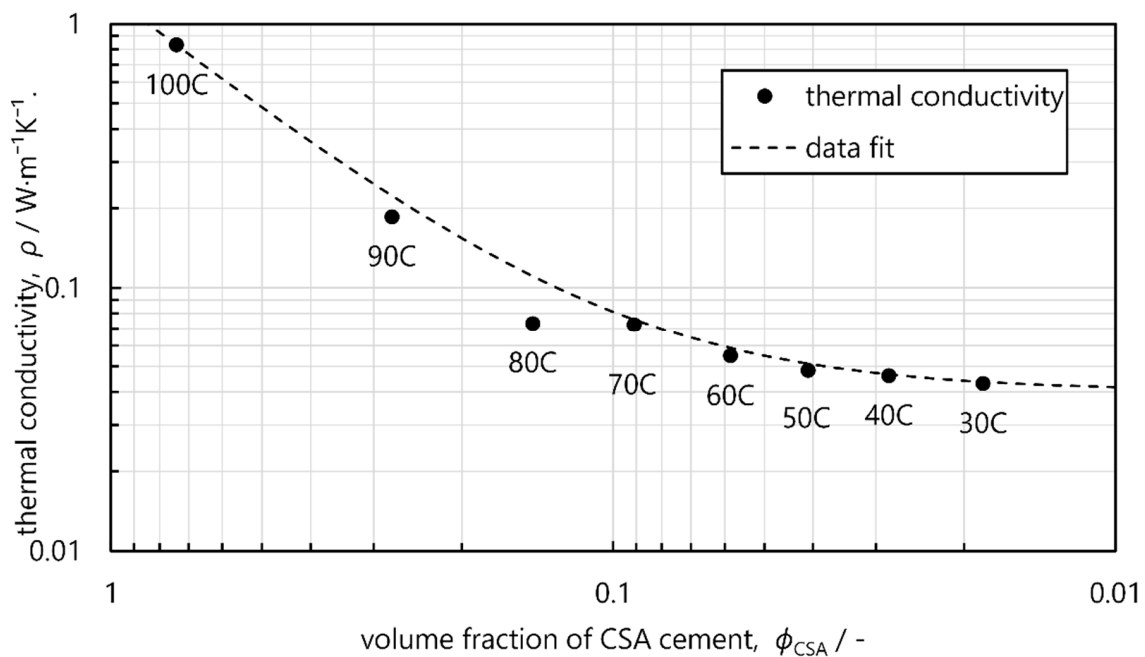


Figure 8. Thermal conductivity as a function of the cement content using surface probes. For each sample composition, a large prism ($N = 1$) was measured at three different spots ($S = 3$). Data fit to $f(\phi) = a_0 + a \cdot \phi^v$, with $a_0 = 0.0404$, $a = 1.234$, and $v = 1.48$.

3.3. Phase Analysis

As already seen from the SEM images in Figures 5 and 6, the hydration of the CSA cement clinker led to the formation of large ettringite crystals that enveloped the HGMSs and formed solid bridges among the spheres when the HGMS content was comparatively low. However, with an increasing amount of HGMSs, the amount of large crystals dropped. In order to thoroughly analyze the differences in phase formation, X-ray diffraction (XRD) was applied.

First, the non-hydrated CSA cement was analyzed. Figure 9 shows the diffractogram of the cement powder, which was investigated at room temperature. The diffractogram shows diffraction peaks of the clinker phases ye'elimite and anhydrite. Ye'elimite is characteristic of CSA cement [24], while anhydrite is added as a sulfate source. Depending on the ratio of these two cement clinker phases, either ettringite (calcium-trisulfate) or calcium-monosulfate will form during hydration, as can be expressed by

$$m = \frac{n_A}{n_Y}, \quad (3)$$

where m is the weight ratio between anhydrite (n_A) and ye'elimite (n_Y). For complete hydration of anhydrite and ye'elimite to ettringite, the ratio m has to be greater than 0.45 [25]. For the used CSA clinker, the ratio was found to be $m = 0.53$ according to Rietveld refinement. Therefore, the formation of ettringite is most likely to happen, at least until the clinker phase ye'elimite is fully depleted.

Figure 10 shows the XRD diffractogram of the hydrated CSA cement (sample 100C), which was prepared using a water/cement ratio of 0.45. Apart from the clinker phases ye'elimite (Y) and anhydrite (A), ettringite (E) was detected as expected from the calculated ratio $m = 0.53$. However, ye'elimite and anhydrite were still present, which can be explained by the relatively short time of hydration of only 14 days. Complete hydration of ye'elimite and anhydrite phases to ettringite would probably take a couple of months or even years. However, the amount of ettringite that had already formed in the first 14 days of hydration led to a high early flexural strength of sample 100C of about 4 MPa, as shown in the above bending tests (Figure 7).

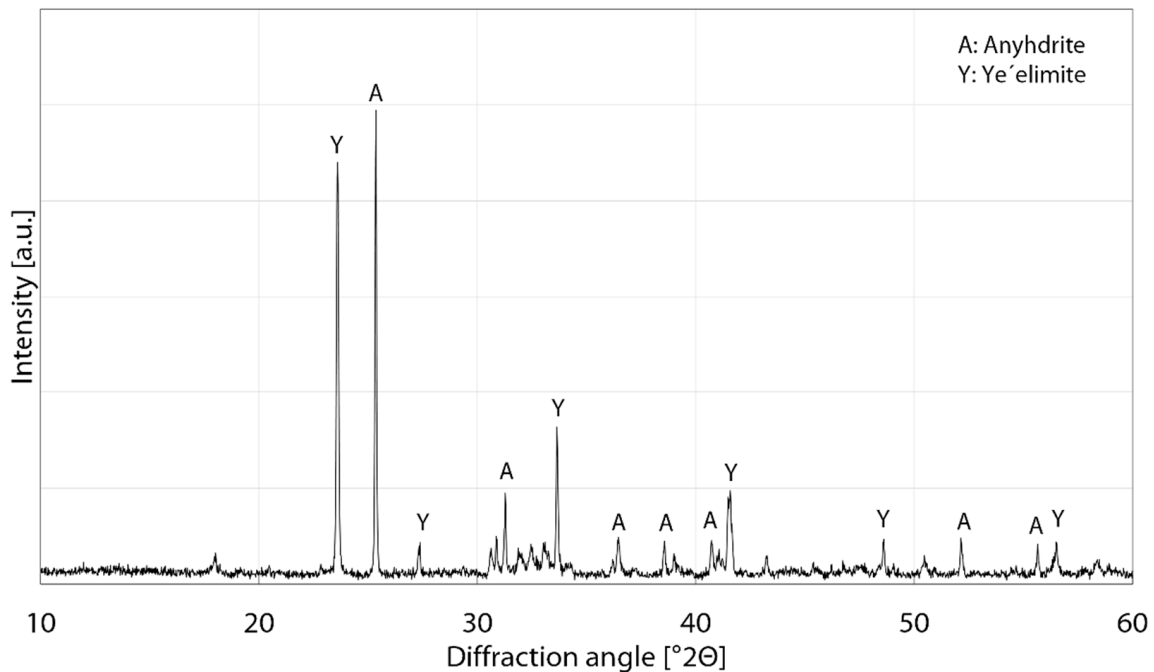


Figure 9. XRD diffractogram of the CSA cement clinker used in this study. The cement was measured as a powder that was stored in a dry environment until the measurement.

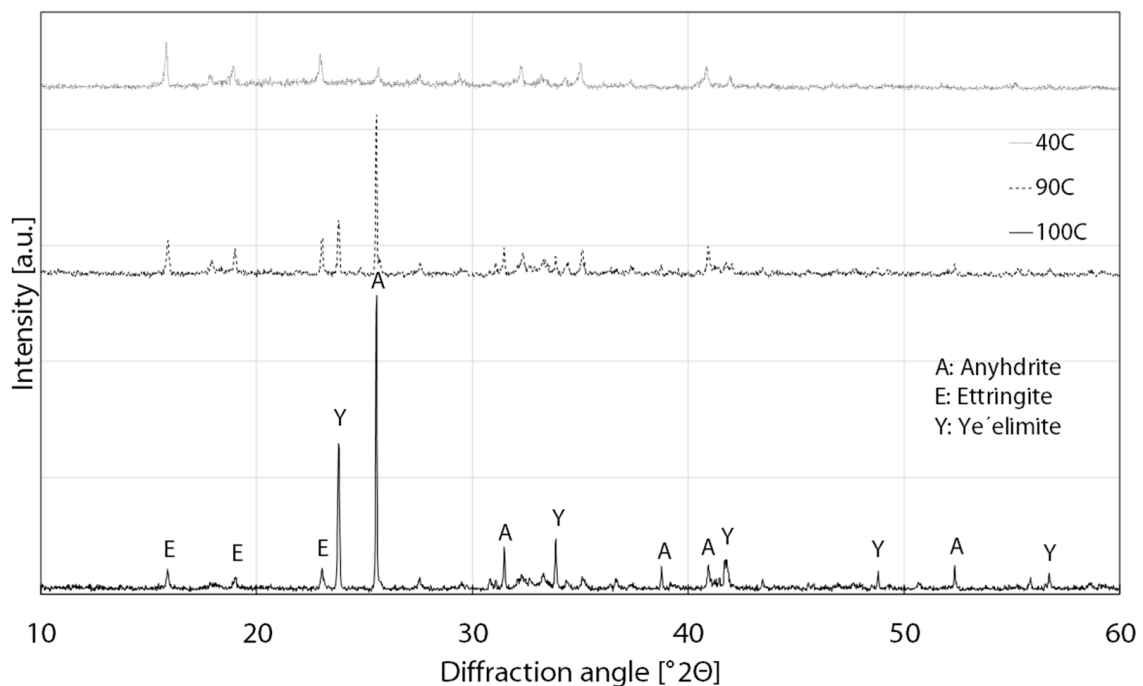


Figure 10. XRD diffractograms of the following samples after 14 days of hydration: 100C (solid line), 90C (dotted line), and 40C (dashed line).

Even though the addition of the amorphous HGMSs reduced the overall intensity of the diffractograms, ettringite formation was easily recognizable for the composite samples. Exemplarily, the diffractograms of samples 90C and 40C are shown in Figure 10. Apart from ettringite, ye'elimite as well as anhydrite were still detected. However, the peak intensities for ye'elimite (Y) and anhydrite (A), e.g., at $23.5^\circ 2\theta$ (Y) or $26^\circ 2\theta$ (A), decreased clearly (sample 90C) or almost vanished (see Y in sample 40C), while the ettringite ϵ peaks, e.g., at $16^\circ 2\theta$, clearly stand out. We assume that the ettringite formation is, on the

one hand, preferred by the increasing water–cement ratio, and on the other hand by the huge amount of surface area that is provided by the HGMSs and which is presumably a preferred place for nucleation of ettringite crystals. Considering that nucleation outweighs the crystal growth of ettringite with an increasing amount of HGMSs, it could explain the decreasing proportion of those large needle-like ettringite crystals in the SEM micrographs in Figures 5 and 6. Ettringite was still the dominant crystal phase and was present even at high fractions of added HGMSs, but its crystal growth was retarded. The crystallite size, calculated by using the Scherrer equation [26] utilizing the peaks' width measured for the Ettringite peak at $2\theta = 16^\circ$ for the specimens 100C and 30C, shows a decrease by around 50% from 96 nm in sample 100C to 45 nm in sample 30C. Overall, the hydration seemed to be faster with the addition of HGMSs as the ye'elimite phase almost vanished after 14 days of hydration in sample 40C, while sample 100C still contained a considerable fraction of ye'elimite after the same period of time.

4. Conclusions and Outlook

Our investigations aimed at characterizing a two-component lightweight composite mortar consisting of hollow glass microspheres (HGMSs) and CSA cement as the binder with varying amounts of the components. After mixing and casting, the prepared prisms rested for 14 days under a controlled temperature and moisture to achieve hydraulic setting. The prepared samples were finally characterized in terms of porosity, density, flexural strength, thermal conductivity, and phase formation.

As expected, the addition of HGMSs led to a decrease in the density, flexural strength, and thermal conductivity of the solidified composites. Each of the parameters dropped by approximately one order of magnitude by increasing the amount of HGMSs from zero to 70 wt.%. By contrast, the open porosity of the solidified samples was only somewhat influenced by the addition of HGMSs, as the open porosity was increased from about 25% without addition of HGMSs to 32% with 70 wt.% of HGMSs. Generally, the properties of the solidified composites should be considered as a three-component system consisting of cement, HGMSs, and porosity (air), while the remaining water is mainly chemically bound to the cement phases. The material properties of the composite might be interpolated by the volume-related contribution of each of these components by the help of mathematical mixing rules. While the trend of the curves for bulk density, flexural strength, and thermal conductivity indicated some non-linearity, a power-law-based mixing rule is justified.

Micrographs and phase analysis demonstrated that, in composites with up to 50 wt.% of HGMSs, the spheres were surrounded by a void-filling, loose network of large, up to 10- μm -long, needle-like ettringite crystals. Ettringite is the preferred hydration product according to the given ratio of anhydrite and ye'elimite in the clinker. With an increasing amount of HGMSs, the network of large crystals gradually vanished. The decrease in the embedding matrix phase was accompanied with a loss of mechanical strength and heat conduction, respectively. Micrographs revealed that at high loads of HGMSs (60 or 70 wt.%), the glass spheres were covered predominantly by tiny ettringite seed crystals instead of columnar crystals. Phase analysis confirmed, however, that ettringite formation was proportionally even more pronounced at high loads of HGMSs. Therefore, we conclude that the high surface area provided by HGMSs contributed preferentially to heterogeneous nucleation of ettringite on the glass surface at the expense of crystal growth. The increase in nucleation rate led to an even faster consumption of the cement phases ye'elimite and anhydrite. Hence, the clinker phases, such as ye'elimite, almost vanished after 14 days of hydration. In contrast, the mixtures containing less HGMSs still contained a considerable share of ye'elimite after the same period of time.

The mixture of CSA cement and HGMSs generally meets the requirements for a lightweight insulating plaster. Compositions consisting of 50 to 60 wt.% of HGMSs are lightweight with densities ranging from 0.15 to 0.2 $\text{g}\cdot\text{cm}^{-3}$ and heat-insulating with thermal conductivities ranging from 0.043 to 0.046 $\text{W}\cdot\text{m}^{-1}\text{K}^{-1}$, while also offering a sufficient flexural strength of 0.4 to 0.5 MPa for facade application. The thermal conductivity ap-

proaches that of the most commonly used materials for facade insulation, EPS and XPS. The thermal conductivity of EPS ranges from 0.035 to 0.049 $\text{W}\cdot\text{m}^{-1}\text{K}^{-1}$, while its density is about 0.03 $\text{g}\cdot\text{cm}^{-3}$ [7,8]. Due to its purely mineral composition, the HGMS/CSA composites are fire resistant without addition of flame retardants. Its spraying applicability was demonstrated elsewhere [9].

As stated above, a further improvement in thermal insulation to less than 0.040 $\text{W}\cdot\text{m}^{-1}\text{K}^{-1}$ would require the composites to have more open pores. That would necessitate elongated solid bridges among the HGMSs to maintain structural cohesion and thus sufficient mechanical strength. Currently, this seems to be contradictory as high amounts of HGMSs tend to form smaller ettringite crystals as demonstrated in this study. Future work will therefore extend the focus to the hydration process of CSA cements. Our intention is to investigate the dependence of nucleation and crystal growth on secondary phases such as HGMSs. Further, the effect on the interparticular bonding and mechanical strength of the composite plaster will be crucial for improving the plaster's thermal insulating properties.

Author Contributions: Conceptualization, S.Z. and A.R.; methodology, S.Z. and D.H.; validation, A.R., D.H. and T.G.; investigation, S.Z.; writing—original draft preparation, S.Z. and A.R.; writing—review and editing, S.Z., A.R., D.H., T.G., F.S. and S.S.; supervision, S.S. and T.G. All authors have read and agreed to the published version of the manuscript.

Funding: Funded by the Deutsche Forschungsgemeinschaft (DFG, German Research Foundation) (491183248) and the Open Access Publishing Fund of the University of Bayreuth.

Institutional Review Board Statement: Not applicable.

Informed Consent Statement: Not applicable.

Data Availability Statement: The data presented in this study are available on request from the corresponding author. The data are not publicly available due to intellectual properties of the industrial partner, Franken Maxit.

Acknowledgments: The authors would like to thank Max Schmidt (TAZ Spiegelau) for the RFA measurements.

Conflicts of Interest: The authors declare no conflict of interest.

References

1. European Commission. A European Green Deal. Available online: https://ec.europa.eu/info/strategy/priorities-2019-2024/european-green-deal_en (accessed on 11 November 2021).
2. European Environment Agency. Greenhouse Gas Emissions from Energy Use in Buildings in Europe 2021. Available online: <https://www.eea.europa.eu/data-and-maps/indicators/greenhouse-gas-emissions-from-energy/assessment> (accessed on 11 November 2021).
3. Dombaycı, Ö.A.; Gölcü, M.; Pancar, Y. Optimization of insulation thickness for external walls using different energy-sources. *Appl. Energy* **2006**, *83*, 921–928. [CrossRef]
4. Paiho, S.; Seppä, I.P.; Jimenez, C. An energetic analysis of a multifunctional façade system for energy efficient retrofitting of residential buildings in cold climates of Finland and Russia. *Sustain. Cities Soc.* **2015**, *15*, 75–85. [CrossRef]
5. European Commission. In Focus: Energy Efficiency in Buildings. Available online: https://ec.europa.eu/info/news/focus-energy-efficiency-buildings-2020-feb-17_en (accessed on 11 November 2021).
6. Heller, N.; Flamme, S. Waste management of deconstructed External Thermal Insulation Composite Systems with expanded polystyrene in the future. *Waste Manag. Res.* **2020**, *38*, 400–407. [CrossRef] [PubMed]
7. Lakatos, A. Comparison of the Thermal Properties of Different Insulating Materials. *Adv. Mat. Res.* **2014**, *899*, 381–386. [CrossRef]
8. Ellouze, A.; Jesson, D.; Ben Cheikh, R. The effect of thermal treatment on the properties of expanded polystyrene. *Polym. Eng. Sci.* **2020**, *60*, 2710–2723. [CrossRef]
9. Lehmann, S.; Schwinger, L.; Scharfe, B.; Gerdes, T.; Ehrhardt, M.; Riechert, C.; Fischer, H.-B.; Schmidt-Rodenkirchen, A.; Scharfe, F.; Wolff, F. Mikro-Hohlglaskugeln als Basis energieeffizienter Dämmung von Gebäuden. In *HighTechMatBau—Neue Werkstoffe für Urbane Infrastrukturen, Proceedings of the Beiträge der Konferenz für Neue Materialien im Bauwesen, Berlin, Germany, 31 January 2018*, 1st ed.; Fraunhofer IRB Verlag: Stuttgart, Germany, 2018; pp. 21–25. ISBN 9783738800821. (In German)

10. Shahedan, N.F.; Al Bakri Abdullah, M.M.; Mahmed, N.; Kusbiantoro, A.; Tammam-Williams, S.; Li, L.-Y.; Aziz, I.H.; Vizureanu, P.; Wysłocki, J.J.; Błoch, K.; et al. Properties of a New Insulation Material Glass Bubble in Geo-Polymer Concrete. *Materials* **2021**, *14*, 809. [CrossRef] [PubMed]
11. Martín, C.M.; Scarponi, N.B.; Villagrán, Y.A.; Manzanal, D.G.; Piqué, T.M. Pozzolanic activity quantification of hollow glass microspheres. *Cem. Concr. Compos.* **2021**, *118*, 103981. [CrossRef]
12. Schneider, M. The cement industry on the way to a low-carbon future. *Cem. Concr. Res.* **2019**, *124*, 105792. [CrossRef]
13. Bullard, J.W.; Jennings, H.M.; Livingston, R.A.; Nonat, A.; Scherer, G.W.; Schweitzer, J.S.; Scrivener, K.L.; Thomas, J.J. Mechanisms of cement hydration. *Cem. Concr. Res.* **2011**, *41*, 1208–1223. [CrossRef]
14. Shi, C.; Jiménez, A.F.; Palomo, A. New cements for the 21st century: The pursuit of an alternative to Portland cement. *Cem. Concr. Res.* **2011**, *41*, 750–763. [CrossRef]
15. Hanein, T.; Galvez-Martos, J.-L.; Bannerman, M.N. Carbon footprint of calcium sulfoaluminate clinker production. *J. Clean. Prod.* **2018**, *172*, 2278–2287. [CrossRef]
16. Winnefeld, F.; Lothenbach, B. Hydration of calcium sulfoaluminate cements—Experimental findings and thermodynamic modelling. *Cem. Concr. Res.* **2010**, *40*, 1239–1247. [CrossRef]
17. Na, O.; Kim, K.; Lee, H.; Lee, H. Printability and Setting Time of CSA Cement with Na₂SiO₃ and Gypsum for Binder Jetting 3D Printing. *Materials* **2021**, *14*, 2811. [CrossRef] [PubMed]
18. Chaunsali, P.; Mondal, P. Influence of Calcium Sulfoaluminate (CSA) Cement Content on Expansion and Hydration Behavior of Various Ordinary Portland Cement-CSA Blends. *J. Am. Ceram. Soc.* **2015**, *98*, 2617–2624. [CrossRef]
19. 3M. Datasheet 3M Glass Bubbles K Series, S Series and iM Series. Available online: <https://multimedia.3m.com/mws/media/910490/3m-glass-bubbles-k-s-and-im-series.pdf> (accessed on 2 December 2021).
20. DIN EN 196-1:2016-11; Prüfverfahren für Zement_-Teil_1: Bestimmung der Festigkeit; Deutsche Fassung EN_196-1:2016; Beuth Verlag GmbH: Berlin, Germany, 2016.
21. DIN 66137-2:2019-03; Bestimmung der Dichte fester Stoffe_-Teil_2: Gaspyknometrie; Beuth Verlag GmbH: Berlin, Germany, 2019.
22. Doebelin, N.; Kleeberg, R. Profex: A graphical user interface for the Rietveld refinement program BGMN. *J. Appl. Crystallogr.* **2015**, *48*, 1573–1580. [CrossRef]
23. Lemmon, E.W.; Jacobsen, R.T. Viscosity and Thermal Conductivity Equations for Nitrogen, Oxygen, Argon, and Air. *Int. J. Thermophys.* **2004**, *25*, 21–69. [CrossRef]
24. Jeong, Y.; Hargis, C.W.; Kang, H.; Chun, S.-C.; Moon, J. The Effect of Elevated Curing Temperatures on High Ye’elite Calcium Sulfoaluminate Cement Mortars. *Materials* **2019**, *12*, 1072. [CrossRef]
25. Trauchessec, R.; Mechling, J.-M.; Lecomte, A.; Roux, A.; Le Rolland, B. Impact of anhydrite proportion in a calcium sulfoaluminate cement and Portland cement blend. *Adv. Cem. Res.* **2014**, *26*, 325–333. [CrossRef]
26. Muniz, F.T.L.; Miranda, M.A.R.; Morilla Dos Santos, C.; Sasaki, J.M. The Scherrer equation and the dynamical theory of X-ray diffraction. *Acta Cryst. A* **2016**, *72*, 385–390. [CrossRef] [PubMed]